On-Orbit Pile-Up Detection and Digital Pulse Shape Measurement Results in the Radiation Telescope

Haruka Ueno, Koki Kamiya, Haruhisa Matsumoto, Makoto Tomitaka, and Takeshi Takashima

***Abstract*— We have developed a radiation environment monitor called the Technical Data Acquisition Equipment (TEDA) installed in the RAPid Innovative payload demonstration Satellite 1 (RAPIS-1) which was launched on January 18, 2019. The TEDA measured the energy spectra of electrons, protons, and He ions. In addition to the functions of a conventional sensor, we added a fast digital sampling function to the TEDA. The operational verification in orbit was successful, and the pile-up waveform signal was acquired for the first time at The Japan Aerospace Exploration Agency (JAXA). The TEDA also obtained data showing that pile-up detection also worked properly.**

***Index Terms*— Energy measurement, radiation detector circuits, radiation monitoring, space radiation.**

I. Introduction

AN UNDERSTANDING of the radiation environment in space is essential for safe space activities. Space radiation models developed from extensive satellite data can help designers estimate the worst case environment for a satellite. Current and near-real-time radiation environment data will tell satellite operators and astronaut-supporting controllers whether the "space weather" is quiet or active.

The history of measurement technology for charged particles such as protons and electrons of the radiation belts began with the Geiger–Muller counter applied in the 1960s [1]. Currently, scintillation detectors and solid-state detectors have been used commonly. In addition, multiplier detectors are sometimes used to detect small signals such as low-energy charged particles. Magnetic spectrometers, which use magnetic fields generated in the instrument, are suitable for discriminating between ions and electrons [2]. The Japan Aerospace Exploration Agency (JAXA) has been developing a particle energy spectrometer using solid-state sensors suitable for measuring electrons, protons, α-particles, and heavy ions, since each particle of space radiation has different effects on onboard equipment and the human body [3]–[5].

In typical components of radiation signal-processing circuits, there is first a pre-amplifier that converts the charge generated by the detector into a voltage and then a waveform-shaping amplifier is connected to convert the output into an appropriate waveform pulse. The pulses are then read into a multiple wave-height analyzer to measure the wave-height values, which are then measured as an energy spectrum.

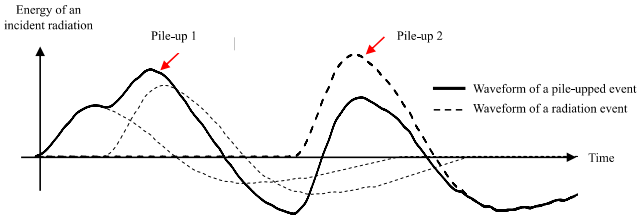

Fig. 1. Cartoon of examples of pile-ups. The second wave changes the true height of the first wave, depending on the timing from the incidence of the first wave.

There is a difficulty in measuring the energy of radiation in an environment with a high count rate. Examples of high count rates in space occur when a spacecraft passes through the South Atlantic Anomaly (SAA) [6]–[8] or when solar flare particles arrive at the spacecraft [9]. To detect radiation with high accuracy, the preamplifier's decay time is designed to be rather long ($\sim$10 μs) in order to collect all charges generated by radiation in a device. However, in an environment with a high count rate, subsequent radiation enters before the preamplifier recovers, and the pulses overlap each other. This phenomenon is called pile-up [10], and it leads to inaccurate energy measurements unless appropriate processing is done. Fig. 1 shows examples of pile-up events. The energy of the particles is overestimated in the example of pile-up 1 and conversely, underestimated in pile-up 2.

JAXA has been conducting research to establish techniques for detecting and then removing pile-up events from measurement sequences. By removing pile-up effects, counting and energy can be correctly measured even at a high count rate. The Technical Data Acquisition Equipment (TEDA) installed on RAPid Innovative payload demonstration Satellite 1 (RAPIS-1) [11] launched on January 18, 2019, can detect pile-ups that occur if a digital sampling circuit is added to the system. This article describes the results of an on-orbit demonstration of the TEDA onboard RAPIS-1.

II. Outline of RAPIS-1/TEDA

The RAPIS-1/TEDA consists of a low-energy electron spectrometer (ELS-A) and a medium-energy alpha and proton

Manuscript received January 21, 2021; revised March 17, 2021 and April 22, 2021; accepted April 28, 2021. Date of publication May 11, 2021; date of current version August 16, 2021.

Haruka Ueno, Koki Kamiya, Haruhisa Matsumoto, and Makoto Tomitaka are with the Japan Aerospace Exploration Agency (JAXA), Tsukuba 305-8505, Japan (e-mail: ueno.haruka@jaxa.jp; kamiya.kohki@jaxa.jp; matsumoto.haruhisa@jaxa.jp; tomitaka.makoto@jaxa.jp;).

Takeshi Takashima is with the Institute of Space and Astronautical Science (ISAS)/JAXA, Sagamihara 252-5120, Japan (e-mail: takashima.takeshi@jaxa.jp).

Color versions of one or more figures in this article are available at https://doi.org/10.1109/TNS.2021.3078515.

Digital Object Identifier 10.1109/TNS.2021.3078515

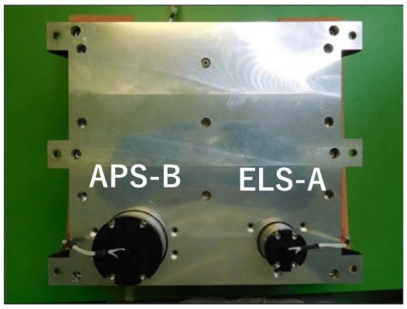

Fig. 2. Exterior photograph of the TEDA. The weight was 3.2 kg and the size was 220 mm × 184 mm × 92 mm.

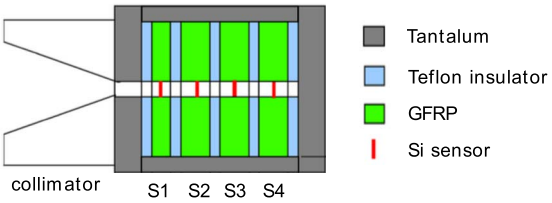

Fig. 3. Cartoon of simplified cross section of ELS-A and APS-B. Each sensor consists of four silicon semiconductors. The two sensors have a common structure except for the thickness of S1.

TABLE I
PROPERTIES OF MEASUREMENTS OF THE TEDA

Particle	Terms	Design Value
Electron	Energy range	0.04 – 20 MeV
	Counting ability	1.9×10^5 cps (count per sec)
	Energy channels	21
	Energy resolution	25 keV (FWHM)
	FOV	±20°
Proton	Energy range	1.2– 250 MeV
	Counting ability	2.2×10^5 cps
	Energy channels	12
	Energy resolution	0.4 MeV (FWHM)
	FOV	±25.4°
He	Energy range	6.38 – 400 MeV
	Counting ability	2.2×10^5 cps
	Energy channels	10
	Energy resolution	1.6 MeV (FWHM)
	FOV	±25.4°
Heavy ion	LET range	2.8 - 10^3 MeV cm^2/g
	Channels	6
		LET0: 2.8 – 6.4 MeV cm^2/g
		LET1: 6.5 – 40.2 MeV cm^2/g
		LET2: 40.3 – 154.5 MeV cm^2/g
		LET3: 154.6 – 238.2 MeV cm^2/g
		LET4: 238.3 – 279.0 MeV cm^2/g
		LET5: 280 – 1000 MeV cm^2/g

spectrometer (APS-B). Fig. 2 shows an external view of the TEDA. The signal processors and the interface to the satellite system are the same for both sensors. Fig. 3 shows a cross section of ELS-A and APS-B. Table I summarizes the performance of both sensors. The full-width at half-maximum (FWHM) values for each particle were the same for all energy channels. The FWHM is defined by the ADC distribution of the output signal relative to the input of a test pulse with a specific voltage value. These values were determined from the FWHMs of the values from the analog-to-digital converter (ADC) distributions relative to the inputs of determined voltage.

Although the radiation environment of RAPIS-1, which is at an orbital altitude of 500 km, is relatively mild compared to low-earth-orbit satellites, the components used in the TEDA were selected from radiation-hardened or space-proven components. The newly adopted high-speed ADC (ADS4245IRGCT) was confirmed to be tolerant by proton irradiation tests. The ADC used had a resolution of 14 bits, a sampling rate of 160 MS/s, and an effective number of bits equal to 11.5 bits. Regarding total ionizing dose (TID) resistance, most parts are resistant even at 1000 Gy and above. For components for which there is no data on radiation resistance assured by the manufacturer, the TEDA's radiation resistance was confirmed through irradiation tests up to 100 Gy and evaluation of the effectiveness of shielding. To deal with the effects of the single-event upsets (SEUs) that occurred in the field-programmable gate array (FPGA) (A3P600L), the TEDA resets the memory used for processing and measurement data buffering in the FPGA every second. Even if an SEU occurs, the TEDA can return to the normal state by this reset process. The components that can be affected from single-event transients (SETs) are operational amplifiers and ADCs. The TEDA was unaffected by a temporary signal disturbance caused by SETs by setting the trigger condition and the event discrimination condition appropriately. The regulator may also be affected by SETs. Selecting the proper capacitor for the output circuitry ensured that the subsequent circuits would not fail. A single-event latch-up (SEL) can lead to permanent failure after just one occurrence. The threshold of SEL occurrence in the adopted FPGA (A3P600L) is 87.2 MeV cm^2/mg, with a cross section of 2×10^{-7} cm^2/FPGA. Although the frequency of occurrence is extremely low, the TEDA has installed a breaker for power supply and a resistor element for current control on the circuit to prevent electronic components from failing when an SEL occurs. These design guidelines, applied to radiation tolerance, satisfy [12].

A. ELS-A

ELS-A consists of four silicon semiconductor detectors (SSDs). The thickness of the first SSD on top (S1) is 80 μm, and 1500 μm for the other sensors. The bottom sensor (S4) is used to determine the event when a particle has penetrated the sensor. ELS-A determines the energy of the incident electrons. Simulated energy loss at each sensor relative to the incident energy was used to identify particles in ELS-A and to determine the energy channel for electrons. The measured energy at S1 determines the particle type of incident particles. The sum of the measured energy in S1, S2, and S3 determines the energy channel of electrons.

B. APS-B

Four SSDs are also used in APS-B. The first sensor (S1) is a 250-μm-thick SSD, and the other sensors are 1500 μm in

thickness. The bottom sensor (S4) determines whether penetration through the sensor of particles occurs. APS-B determines the type of particle and its energy by applying the $\Delta E - E$ method [13]. The look-up tables (LUTs) were set according to irradiation tests and numerical calculations. The TEDA used the $\Delta E - E$ method to determine a particle and its energy. In both sensors, four silicon semiconductors (SSDs) were used for energy loss detection. The energy loss by incidence of a particle in the first SSD (ΔE), which is a transmissive detector, and the sum of the energy lost in all SSDs (E_{SUM}) were calculated numerically, and the correspondence table of the ADC value of energy loss to the incident energy of the particle was stored in the read only memory (ROM) of the TEDA as LUTs [14]. In the measurement on an orbit, the sensor determined the mass number of particles from the ADC value of ΔE. The energy channel was determined by referring to the LUTs from the ADC value of ΔE and E_{SUM}.

In the Count mode, the APS-B also measures the linear energy transfer (LET) in the range from 2.8 up to 10^3 MeV cm^2/g with six channels (see Table I). The LET measurement starts when both the trigger signal (S1) and the anti-coincidence signal (S4) are detected. The LET channel is determined by dividing the energy value measured in S3 by the sensor thickness, and the count value of the LET channel is incremented.

C. Observation and Calibration Modes

The operational mode of the TEDA has three observation modes (Count mode, List mode, and Waveform mode) and two calibration modes (CAL mode and Dump mode).

The Count mode was used for counting events of each energy channel. The TEDA was mainly operated in the Count mode. To determine the atomic number and energy channel of an incident particle, the DIGITAL FPGA accesses the LUTs of correspondences between incident particles and energies stored in the ROM of the signal processor.

The List mode is used to verify the health of the device. The signal-processing circuits detect peaks from the signal output from the waveform-shaping amplifiers that follow the all-Si detector and outputs the peak ADC values. Using this data, the health is evaluated by verifying the correlation tables determined by ground tests.

The Waveform mode was set for acquisition of digitally sampled waveform data with several sampling rates (48, 36, 24, 12 MHz). In this mode, the waveform data of the signal from each sensor sampled by the fast A/D circuit is the output. This is a new operating mode that has not been used in traditional devices by JAXA.

In the CAL mode, the signal-processing section can generate calibration signals, and outputs from these signals are used for the soundness of the processing circuit following the preamplifier. The Dump mode is used to check and rewrite the LUTs. The LUTs stored in ROM can be downlinked in the Dump mode and the LUTs can be overwritten on command

III. Pile-up Detection Technique

Fig. 4 shows a schematic of the TEDA configuration. The signal from the SSD is input to the peak hold (P/H) circuit after going through the preamplifier and waveform-shaping circuit. The peak hold circuit has the function of holding the maximum value of the voltage value input to the waveform-shaping amplifier. Fig. 5 shows an example of pile-up occurring in a P/H circuit. When a voltage of the signal processed by the main amplifier exceeds the threshold value of V_H, the input signal to the P/H circuit is cut off by a gate signal after the set time (T_α) has elapsed to prevent the occurrence of pile-up. The circuit holds the wave height during this time. After another time (T_β), the gate input signal is released, and the instrument is ready to detect the next signal. However, a pile-up can cause the signal processor to overestimate the energy of the first signal (dotted line in Fig. 5) if the pile-up occurs due to radiation incident before time T_α (dashed line in Fig. 5).

Conventional radiation-measuring instruments developed by JAXA only have P/H circuits. The data measured by our instrument in high count rate regions such as the SAA have been corrected to the true count rate using the dead time of the instrument [15]. However, we have treated them as unreliable data. In order to solve this problem, we developed the logic to detect pile-up events by focusing on the fact that the peaking time and zero-crossing time of the amplifier's bipolar output waveform are theoretically determined uniquely for each incident particle.

The key to solving this problem is the output waveform from the waveform-shaping amplifier circuit, which is a combination of a differentiation circuit (CR circuit) and an integration circuit (*RC* circuit). The baseline of the signal output by the waveform-shaping amplifier circuit may deviate from the true baseline when the interval between radiation incidence is short. This phenomenon is called baseline shift, and it affects energy measurements. The waveform-shaping amplifier circuit of the TEDA adopted the *RC-RC-CR* circuit, which shapes the waveform from the preamplifier into a bipolar form and excludes baseline shift. Applying the Laplace transform [16] to the differential equations for the *RC* and *CR* circuits, respectively, the description of the output voltage from the circuit in the s-domain is expressed as shown in the following equation:

$$V_{\mathrm{out}}(s) = \frac{A_1}{1+\tau_1 s} \cdot \frac{A_2}{1+\tau_2 s} \cdot \frac{A_3 \tau_3 s}{1+\tau_3 s} \cdot V_{\mathrm{in}}(s). \tag{1}$$

The $\tau_1 (= R_1 C_1), \tau_2 (= R_2 C_2)$, and $\tau_3 (= R_3 C_3)$ are time constants of the initial-stage *RC* circuit, the second-stage *RC* circuit, and the third-stage *CR* circuit, respectively, and A_1, A_2, and A_3 are gains of each circuit. Assuming that the pulse width of the radiation signal is sufficiently short compared to time constants of each circuit, any wave height value can be regarded as an impulse signal, and (1) becomes (2).

$$V_{\mathrm{out}}(s) = \frac{A_1}{1+\tau_1 s} \cdot \frac{A_2}{1+\tau_2 s} \cdot \frac{A_3 \tau_3 s}{1+\tau_3 s} \cdot P_{H.} \tag{2}$$

The P_H is the pulse height of an impulse signal. When the gains of all circuits are the same and the time constants have the same value, applying the inverse Laplace transform [16], (2) is transformed into a function of time (t) as shown in the

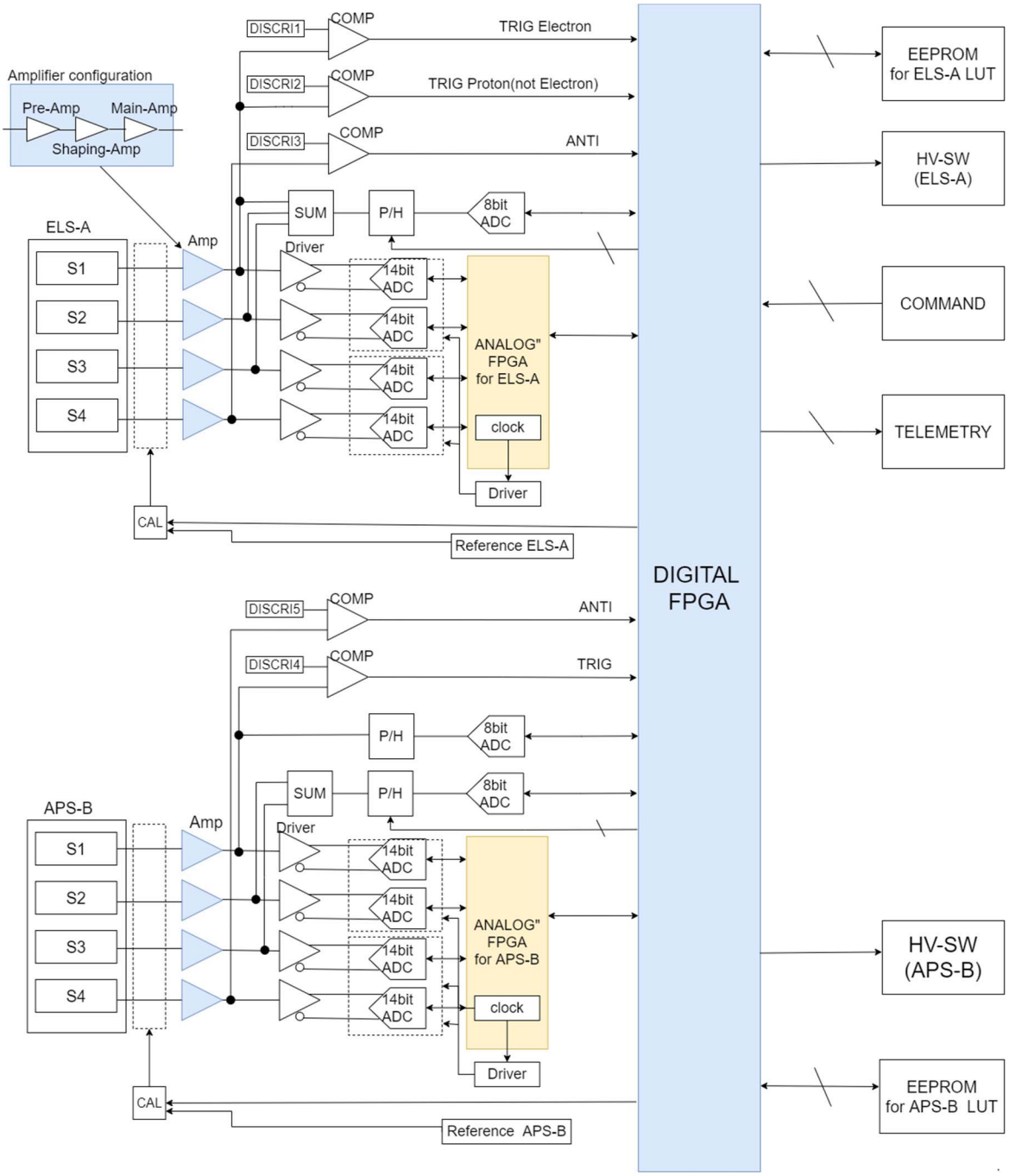

Fig. 4. Block diagram of the TEDA. For the sake of simplicity, the sensor is represented as one. The dotted line is the new processing hardware.

following equation:

$$V_{\text{out}}(t) = P_H \frac{t}{2\tau^2} e^{-t/\tau}\left(2 - \frac{t}{\tau}\right). \tag{3}$$

This waveform expressed by (3) can be drawn as shown in Fig. 6. This waveform has a maximum value at $(2-2^{1/2})\tau$, a minimum value at $(2+2^{1/2})\tau$, and intersects zero at 2τ, which is independent of any wave height value. For convenience of explanation, the time constants are set to the same value, but the waveform for any combination of time constants will also be as shown in Fig. 6. The occurrence of a pile-up event is determined by using the fact that the peak time and zero-crossing time are constant.

The analog FPGA determines pile-up events from the output signal of the high-speed A/D circuit that processes the signal output from S1. The pattern of pile-up detection in the TEDA was divided according to the second signal input timing. The first pattern was when the signal comes before the crossover timing (COT) or when the signal enters at approximately the same time as the COT. If the state of the comparator signal was on at the time of COT or if the time that state was on was longer than a predetermined value, the analog FPGA detected that a pile-up had occurred. In this case,

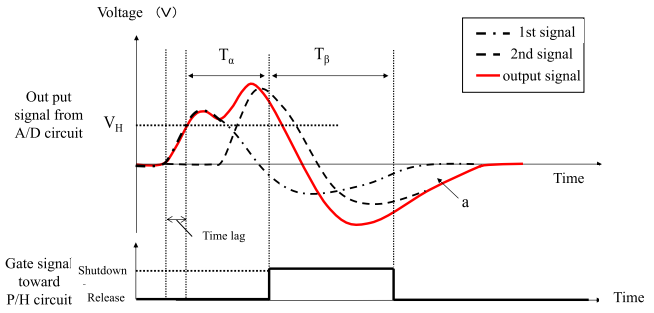

Fig. 5. Cartoon of an example of a conventional radiation measurement sequence with a P/H circuit. In order not to detect pile-up, the measurement is blocked by the gate signal while maintaining the height value of the first wave. However, if the pile-up occurs before the gate signal, the wrong value will be detected.

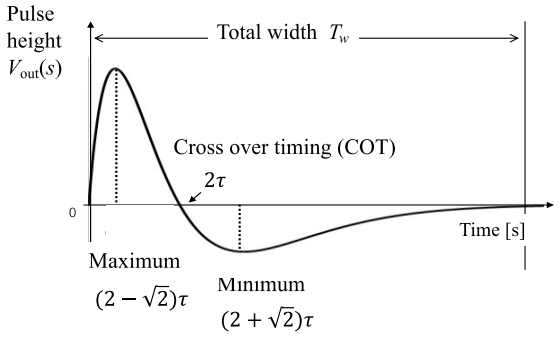

Fig. 6. Diagram of (3) plotted as time on the horizontal axis and voltage on the vertical axis.

the pile-up count and the total count were output with the same value. In another pattern, the analog FPGA determined that a pile-up occurred if the comparator status was turned on twice during the processing time and beyond the COT. In this case, the analog FPGA does not process the second wave as an event and notifies the DIGITAL FPGA that a pile-up event has occurred. The DIGITAL FPGA increments the pile-up count. The total count was twice the value of the pile-up count. In both patterns, the dead time was extended when a pile-up was detected.

The first radiation measurement detector in JAXA equipped with this logic in the RAPIS-1/TEDA was demonstrated on orbit. The RAPIS-1/TEDA also has a fast analog-to-digital conversion circuit (A/D) to measure the waveform output from the main amplifier.

IV. Calibration and Performance Verification by Ground Testing

In this section, we report on the evaluation results of the pile-up detection function and the fast A/D circuit that were added to the TEDA.

A. Evaluation of Pile-up Detection Function

We evaluated the soundness of the pile-up detection function by varying the input time difference between the first and second signals (Δt), as shown in Fig. 7. The pulse repetition frequency (PRF) of the pulse generator was set to 40,006.4 Hz.

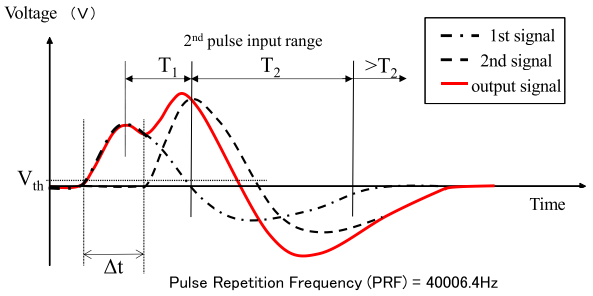

Fig. 7. Cartoon of test condition for pile-up detection of TEDA. Here, T1 is the second pulse input timing from the peaking time to zero crossing time, and T2 is the second pulse input timing from zero-crossing time to tail time of first pulse, corresponding to T_β described in Section III. T1 or T2 for ELS-A and APS-B are different, depending on the time constant of each of its circuits.

TABLE II
Test Results of Pile-up Detection Function

Sensor	Δt (μsec)	Range	Pile-up count (PC)	Total count (TC)
ELS-A	1.0	T1	40006	40006
	1.3		40006	40006
	1.5	T2	40006	80013
	2		40006	80013
	5		40006	80013
	5.2		20043	80013
	5.4	> T2	0	80013
	6		0	80013
APS-B	1	T1	40006	40006
	1.4		40006	40006
	1.5	T2	40006	80013
	2		40006	80013
	4		40006	80013
	4.8		39736	80013
	5	> T2	0	80013
	6		0	80013

Table II shows the test results of the evaluation. The pile-up counter (PC) denotes the number of pile-up detections, and the total counter (TC) denotes the number of trigger detections that are counted when the input signal exceeds the discrimination voltage (V_{th}). The time to the input of the second wave is represented by ΔT, and T_1 and T_2 are the COT of the first wave and the time from the COT to the return to baseline, respectively. The input timing of the second wave was varied slightly as shown in Table II to evaluate the relationship between the pile-up counts and the total counts. In the case of the T_1 range shown in Fig. 7, the PC and TC successfully indicated 40006 which is the same as the PRF. In the T_2 range, it was successfully indicated that the PC was the same as the PRF and that the TC was twice that of the PRF because of double triggering. In the case of exceeding T_2 ($>T_2$), no pile-up was detected and the TEDA operated normally. Note that the peak value of the first signal was successfully detected in all cases.

B. Irradiation Tests

Table III is the list of irradiation tests conducted to demonstrate the function of the TEDA. To confirm the performance

TABLE III
LIST OF FACILITIES FOR IRRADIATION TESTS

Sensor	Particle	Energy	Date	Facility
ELS-A	Elec-tron	300 keV – 2 MeV	2017/8/22-25	JAXA/Tsukuba Space Centor [17] Van de Graaf
APS-B	Proton He	230 MeV 230 MeV/n	2017/6/13-14	NIRS[18] HIMAC
APS-B	Fe	500 MeV/n	2017/7/18	NIRS HIMAC

of the peak-hold and fast A/D circuits, respectively, and to perform an energy calibration of APS-B, the TEDA was irradiated with 100-MeV protons and 230-MeV/n He. The irradiation was carried out at Heavy-Ion Medical Accelerator in Chiba (HIMAC) in the National Institute of Radiological Sciences (NIRS). It confirmed the normality of the particle identification function in both circuits. However, in both circuits, the experimental data of deposited energy in S1 was higher than the simulated value in the experiment. In the circuit design, the detection of the trigger and the determination of the energy channel by the LUTs may not be accurate. Therefore, after the irradiation test, the circuit parameters following S1 were readjusted, and it was confirmed that the irradiation data and the simulation results were consistent. The validity of the S1 gain adjustment results was confirmed in the detection of protons and helium generated as secondary particles in the Fe irradiation tests. ELS-A was calibrated by electron irradiation from 300 keV to 2 MeV.

V. MEASUREMENT RESULTS

RAPIS-1 was launched on January 18, 2019, and the TEDA was put into a 500-km orbit and powered on January 29, 2019. RAPIS-1 was a satellite for on-orbit demonstration of components and equipment developed by companies or JAXA. The TEDA operated normally until January 31, 2020, when the steady-state operation of RAPIS-1 terminated because the on-orbit demonstration of all the instruments aboard RAPIS-1 was completed.

A. Energy Resolution

The operational mode of the TEDA includes a calibration mode (CAL mode). This mode can output the ADC distribution of the output wave height by inputting some specified electrical signals simulating radiation to the silicon detectors. The dispersion of the distribution determines the energy resolution of the detectors. Defining the energy resolution in terms of FWHM of these distributions, the energy resolutions were 22.0 keV for the PH circuit and 23.4 keV for the fast A/D circuit in ELS-A. In APS-B, the energy resolution of the P/H circuit was 0.144 MeV and that of the fast A/D circuit was 0.196 MeV.

B. Evolution of the Pile-up Detection

Comparing the geographic distribution of the total count and the pile-up counts qualitatively assesses whether the pile-up detection logic was working properly. Fig. 8 shows the geographic distribution of the total counts of ELS-A from April 1 to 7, 2019, and shows that of the pile-up counts. Similarly, Fig. 9 shows the figures for APS-B. These figures indicate that the pile-up count was higher in high-count rate areas such as the SAA and polar regions than in other areas.

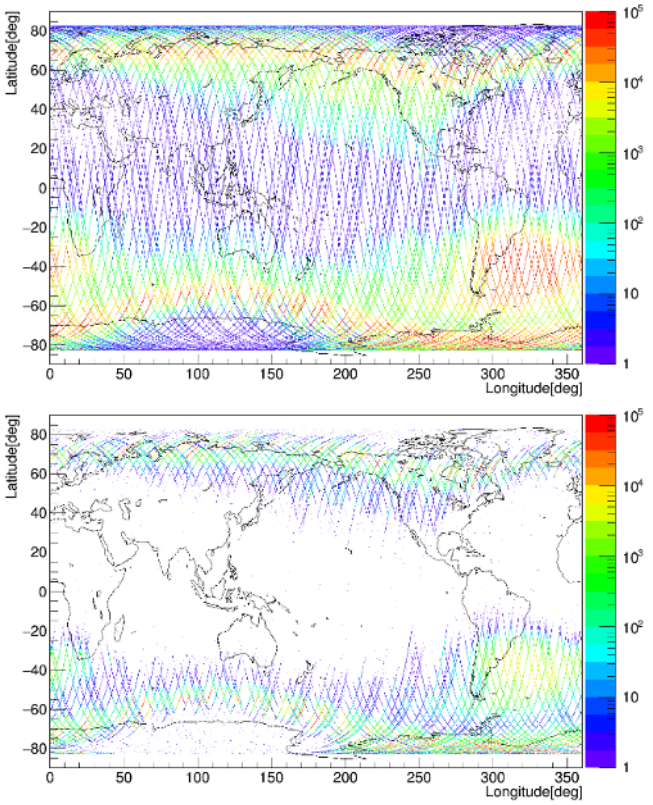

Fig. 8. Geographical distribution of electron fluxes observed by ELS-A (top) and the number of pile-up counts (bottom). The color bar indicates the total count for a given period of time.

At the limit where pile-ups rarely occur relative to the total count, the rate of counting with pile-ups depends on the square of the rate of true event occurrence. Using the least-squares method, both correlations were confirmed to be approximated by a quadratic function. Fig. 10 shows the correlation between the total count and the pile-up count, and this correlation was found to be approximated by the square. This result also supports the correctness of the TEDA's pile-up detection logic.

The fast A/D circuit in the TEDA has a mode to acquire the waveform data, and JAXA acquired the piled-up waveform data for the first time. Fig. 11 shows examples of the pile-up waveforms measured on orbit obtained in the Waveform mode. The top waveform in Fig. 10 corresponds to pile-up 1 in Fig. 1, and the bottom waveform in Fig. 10 corresponds to pile-up 2 in Fig. 1.

C. Comparison With the Radiation Models

Here, a method of converting the count rate acquired by the P/H circuit and the high-speed A/D circuit into a flux will be described. In the P/H circuit, the flux was calculated by the following formula:

$$F_k = \frac{C_k}{1 - c_k \tau} G_k \tag{4}$$

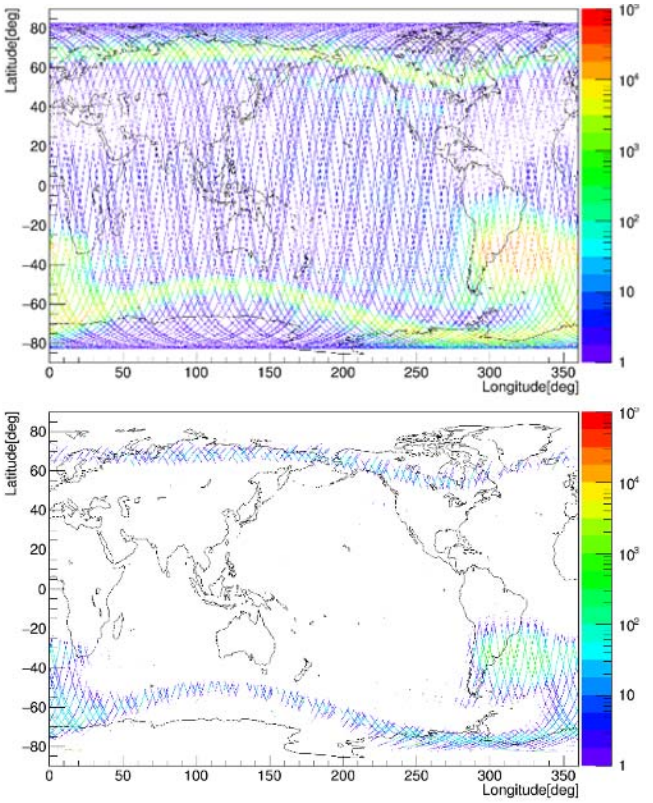

Fig. 9. Geographical distribution of proton fluxes observed by APS-B (top) and the number of pile-up counts (bottom). The color bar indicates the total count for a given period of time.

where F_k is the flux value of the k channel ($\mathrm{cm^{-2}s^{-1}str^{-1}MeV^{-1}}$), C_k is the counting rate of the k channel ($\mathrm{s^{-1}}$), τ is deadtime (2×10^{-5} s), and G_k is the geometric factor and represents the energy response of counter to particle species k. The A/D circuit can detect the pile-up phenomenon, so if the pile-up count value per second is C_p, the actual measurement time t is given by the following:

$$t = \left(1 - \tau C_p\right) \tag{5}$$

where τ is deadtime 5.56×10^{-6}s (ELS-A) and 4.76×10^{-6}s (APS-B). Therefore, the k-channel flux can be calculated with

$$F_k = \frac{C_k}{t} G_k. \tag{6}$$

Fig. 12 shows the comparisons between the electron and proton fluxes measured by the TEDA in the Count mode and those calculated from the radiation belt models (AP8/AE8 [19]–[21] and AP9/AE9 [22]). The measured electron flux below 300 keV is higher than the model value. Since the direction of the TEDA field of view was determined so that the pitch angle of the radiation belt particles on RAPIS-1 orbit was around 90° in all areas, it is reasonable that the flux measured by ELS-A is higher than the model value calculated as the average of omnidirectional flux.

The proton fluxes measured by APS-B are higher than the model values in the energy region above 10 MeV. This difference is apparently due to when particles with sufficient energy to penetrate APS-B incident from outside its field of

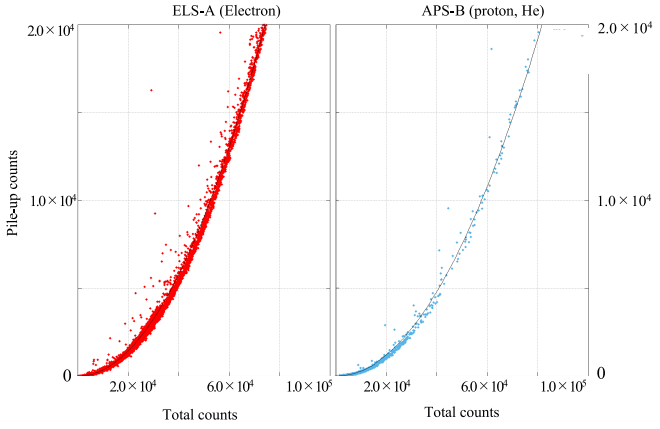

Fig. 10. Correlation between the total count and the pile-up count.

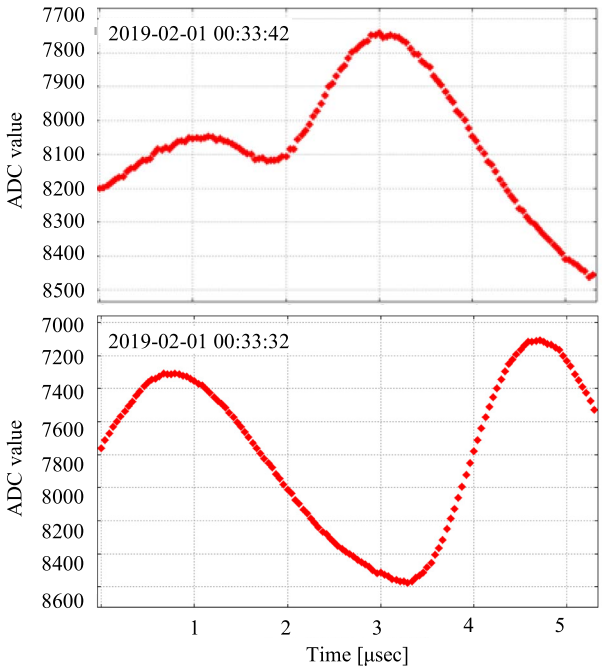

Fig. 11. On-orbit pile-up waveform data detected by the TEDA observation.

view may result in APS-B misidentifying these noise events as true events. This effect becomes non-negligible at small L-values, where the proton energy spectrum shows a wide energy distribution up to high energy such as the SAA. The L-value is the distance between the center of the earth and the point where the magnetic field lines cut the equatorial plane, expressed as the earth's radius. Therefore, the correction to exclude this effect should be based on a more detailed data analysis.

A comparison of the fluxes of P/H and fast A/D circuits in the low-energy region of the electrons shows that the fluxes of fast A/D circuits are higher. The reason the flux of the P/H circuit is low in the low-energy channel is presumed to be due to the measurement error of the energy value caused by pile-up and the reduction of the coefficient rate due to pile-up. On the other hand, there is no difference in the flux due

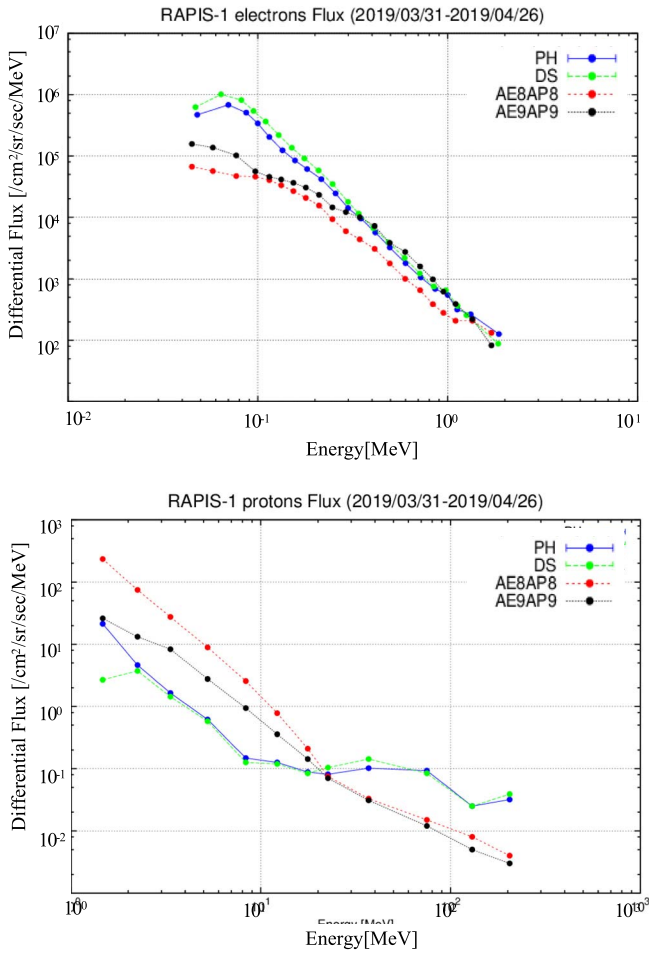

Fig. 12. Comparison of electron fluxes observed in ELS-A (top) and proton fluxes observed in APS-B (bottom) with the radiation belt model. The PH indicates the flux measured by the P/H circuit and DS indicates the flux measured by the fast A/D circuit.

to pile-up because the proton count rate in the radiation band is not large. We note that the extreme difference between the P/H and fast A/D circuits at the first energy channel is due to the wrong table being used to determine the channel, which requires correction in the future.

VI. Conclusion

In order to measure an energy distribution correctly even in a high count rate radiation environment, we installed pile-up detection logic in the RAPIS-1/TEDA. After one year of operation, the TEDA has been operating normally and several data analyses support the correct functioning of the designed pile-up detection logic. Based on the results obtained in RAPIS-1/TEDA, we aim to develop a processing technique for pile-up removal, correction, and a high counting rate ($>10^6$ cps).

Acknowledgment

The authors express their gratitude to Mr. Kagawa for providing the opportunity to install the TEDA on RAPIS-1 and to all those involved in RAPIS-1 and the TEDA who have contributed to development and its operation. This article was performed as a Research Project with Heavy Ions at NIRS-HIMAC.

References

[1] J. A. Van Allen, C. E. McIlwain, and G. H. Ludwig, "Radiation observations with satellite 1958 EX," *J. Geophys. Res.*, vol. 64, pp. 271–286, Mar. 1959.

[2] M. Walt, "Particle fluxes, distribution functions and radiation belt measurements," in *Introduction to Geomagnetically Trapped Radiation*. Cambridge, MA, USA: Cambridge Univ. Press, 1994, pp. 59–91.

[3] Y. Sasaki, H. Matsumoto, T. Goka, T. Nakamura, K. Terasawa, and H. Kitamura, "Technical data acquisition equipment for GOSAT," in *Proc. 30th Int. Cosmic Ray Conf. (ICRC)*, Yuanlin City, Jan. 2007, pp. 643–646.

[4] T. Obara *et al.*, "Space environment data acquisition with the kibo exposed facility on the international space station (ISS)," *Data Sci. J.*, vol. 8, pp. IGY76–IGY84, Mar. 2010, doi: 10.2481/dsj.SS_IGY-007.

[5] H. Matsumoto *et al.*, "Compact, lightweight spectrometer for energetic particles," *IEEE Trans. Nucl. Sci.*, vol. 48, no. 6, pp. 2043–2049, Dec. 2001.

[6] H. Koshiishi and H. Matsumoto, "Space radiation environment in low earth orbit during solar-activity minimum period from 2006 through 2011," *J. Atmos. Solar-Terr. Phys.*, vol. 99, pp. 129–133, Jul. 2013, doi: 10.1016/j.jastp.2012.09.004.

[7] L. J. Lanzerotti and D. N. Baker, "Space weather research: Earth's radiation belts," *Space Weather*, vol. 15, no. 6, pp. 742–745, Jun. 2017.

[8] S. Aleksandrin, S. Koldashov, A. M. Galper, and T. Zharaspayev, "The south atlantic anomaly drift on the proton flux data of satellite experiments," in *Proc. 34th Int. Cosmic Ray Conf. (ICRC)*, Aug. 2016, p. 89, doi: 10.22323/1.236.0089.

[9] D. F. Smart and M. A. Shea, "A review of solar proton events during the 22nd solar cycle," *Adv. Space Res.*, vol. 30, no. 4, pp. 1033–1044, Nov. 2002, doi: 10.1016/s0273-1177(02)00497-0.

[10] S. Usman and A. Patil, "Radiation detector deadtime and pile up: A review of the status of science," *Nucl. Eng. Technol.*, vol. 50, no. 7, pp. 1006–1016, Oct. 2018, doi: 10.1016/j.net.2018.06.014.

[11] Japan Aerospace eXplanation Agency. *Innovative Satellite Technology Demonstration Program*. Accessed: Jan. 20, 2020. [Online]. Available: https://global.jaxa.jp/projects/sat/innovative/

[12] *Space Systems—Evaluation of Radiation Effects on Commercial-off-the-Shelf (COTS) Parts for use on low-Orbit Satellite*, Standard 21980, ISO, Jan. 2020, p. 2020.

[13] A. G. Seamster, R. E. L. Green, and R. G. Korteling, "Silicon detector ΔE, E particle identification: A theoretically based analysis algorithm and remarks on the fundamental limits to the resolution of particle type by ΔE, E measurements," *Nucl. Instrum. Methods*, vol. 145, no. 3, pp. 583–591, Sep. 1977, doi: /10.1016/0029-554X(77)90590-0.

[14] J. Kikuchi, H. Matsumoto, H. Koshiishi, T. Nozaki, and S. Takehisa, "Charged particle measuring apparatus," U.S. Patent 2003158678 A1, Aug. 21, 2003.

[15] G. F. Knoll, "Dead time," in *Radiation Detection and Measurement*, vol. 7, 4th ed. New York, NY, USA: Wiley, 2010, ch. 4, sec. 7, pp. 121–128.

[16] G. F. Knoll, "Pulse shaping," in *Radiation Detection and Measurement*, vol. 1, 4th ed. New York, NY, USA: Wiley, 2010, ch. 17, sec. 1, pp. 625–640.

[17] Aeronautical Technology Directorate. *How do Satellite Failures Relate to the Space Environment?*. Japan Aerospace eXplanation Agency. Accessed: Mar. 16, 2021. [Online]. Available: https://www.aero.jaxa.jp/eng/publication/magazine/sora/2009_no30/ss?2009no30_01.html

[18] Quantum Medical Science Directorate. *Call for Proposal of Experiments at 'HIMAC'*. National Institutes for Quantum and Radiological Science and Technology. Accessed: Mar. 16, 2021. [Online]. Available: https://www.qst.go.jp/site/nirs-english/20559.html

[19] S. F. Fung, "Recent development in the NASA trapped radiation models," in *Radiation Belts: Models and Standards*. Washington, DC, USA: American Geophysical Union, 1996, pp. 79–92.

[20] D. M. Sawyer and J. I. Vette, "AP-8 trapped proton environment for solar maximum and solar minimum," NASA, Greenbelt, MD, USA, Tech. Rep. N–77–18983, 1976.

[21] J. I. Vette, "The AE-8 trapped electron model environment," NASA, Greenbelt, MD, USA, Tech. Rep. NSSDC/WDC-A-RS-91-24, 1976.

[22] G. P. Ginet *et al.*, "AE9, AP9 and SPM: New models for specifying the trapped energetic particle and space plasma environment," *Space Sci. Rev.*, vol. 179, nos. 1–4, pp. 579–615, Mar. 2013, doi: 10.1007/s11214-013-9964-y.